

# Optical Engineering

OpticalEngineering.SPIEDigitalLibrary.org

## Space targets adaptive optics images blind restoration by convolutional neural network

Jianlin Shi  
Rongzhi Zhang  
Shiping Guo  
Yikang Yang  
Rong Xu  
Wei Niu  
Jisheng Li

**SPIE.**

Jianlin Shi, Rongzhi Zhang, Shiping Guo, Yikang Yang, Rong Xu, Wei Niu, Jisheng Li, "Space targets adaptive optics images blind restoration by convolutional neural network," *Opt. Eng.* **58**(9), 093102 (2019), doi: 10.1117/1.OE.58.9.093102.

# Space targets adaptive optics images blind restoration by convolutional neural network

Jianlin Shi,<sup>a,b</sup> Rongzhi Zhang,<sup>a,b</sup> Shiping Guo,<sup>c,\*</sup> Yikang Yang,<sup>a</sup> Rong Xu,<sup>b</sup> Wei Niu,<sup>a</sup> and Jisheng Li<sup>a</sup>

<sup>a</sup>Xi'an Jiaotong University, School of Electronic and Information Engineering, Xi'an, China

<sup>b</sup>State Key Laboratory of Astronautic Dynamics, Xi'an, China

<sup>c</sup>Northwestern Polytechnical University, School of Automation, Xi'an, China

**Abstract.** To obtain sharp images of space targets, high-accuracy restoration of degraded images corrected by an adaptive optics (AO) system is necessary. Existing algorithms are mainly based on the physical constraints of both image and point-spread function (PSF), which are usually continuously estimated in an alternately iterative manner and take a long time to restore blurred images. We propose an end-to-end blind restoration method for ground-based space target images based on conditional generative adversarial network without estimating PSF. The whole network consists of two parts, generator network and discriminator network, which are used for learning the atmospheric degradation process and achieving the purpose of generating restored images. To train the network, a simulated AO image dataset containing 4800 sharp-blur image pairs is constructed by 80 three-dimensional models of space targets combined with degradation of atmospheric turbulence. Experimental results demonstrate that the proposed method not only enhances the restoration accuracy but also improves the restoration efficiency of single-frame object images. © 2019 Society of Photo-Optical Instrumentation Engineers (SPIE) [DOI: 10.1117/1.OE.58.9.093102]

Keywords: adaptive optics; blind restoration; generative adversarial network; space targets.

Paper 190378 received Mar. 17, 2019; accepted for publication Aug. 14, 2019; published online Sep. 17, 2019.

## 1 Introduction

This paper is devoted to removing atmospheric turbulence blur from single ground-based adaptive optics (AO) images, without information about the point-spread function (PSF) or the sharp images of the space target. This work is generally referred to as blind image deconvolution, deblurring, or restoration, which is a typical ill-posed problem in mathematics.<sup>1–3</sup> Although the atmospheric turbulence blur can be partially removed through the AO system, there are correction residuals considering the complexity and cost of the system. At the same time, the wavefront correction will introduce new noises. Consequently, blind image restoration is crucial postprocessing work for further improving the quality of the space target images. It is of great significance to the detection and identification of space targets and the status monitoring of spacecraft. Currently, there are a number of blind image restoration methods, such as classical methods,<sup>4,5</sup> statistical methods,<sup>6</sup> and regularization methods.<sup>7,8</sup> The existing algorithms are mainly based on the physical constraints of the images and the PSF, or the *priori* probability distribution of the images and statistical model of the noise. They estimate the sharp images and PSF continuously in an alternately iterative manner, which takes a long time relatively to restore single-frame images. Inspired by recent works on image-to-image translation by generative adversarial network (GAN),<sup>9</sup> we treated blind image restoration of space target as a special case of image-to-image translation problem. We present a conditional generative adversarial network (cGAN) to learn the turbulent degradation process and compensate the degradation losses. The input of the neural network is a degraded image, and the output is a directly restored sharp image without estimating the corresponding

PSF, improving the efficiency of single-frame image restoration. The results of blind restoration for degraded images outperform even the methods of better performance in application.

The contributions of this paper are mainly in the following three points. (1) A deep neural network model for AO images restoration is proposed based on cGAN. (2) A simulated image dataset of space targets containing 4800 sharp-blur image pairs is constructed, which can be widely used in training neural networks for postprocessing of space target images. (3) An improved loss function for optimizing the neural network parameters is presented, which obtains better restoration results in precision.

The rest of this paper is organized as follows. A brief overview of the blind restoration methods for AO image and GAN method are presented in Sec. 2. The theory underlying the proposed algorithm and network architecture for space target image blind restoration are described in detail in Sec. 3. Dataset of space target images for training the introduced cGAN network is constructed in Sec. 4. Experiments to verify the performance of the method on test dataset in comparison with the most commonly used techniques are presented in Sec. 5. Finally, Sec. 6 concludes this study.

## 2 Related Works

### 2.1 Adaptive Optics Image Restoration

Space target images acquired via ground-based AO telescopes are essentially blurred by atmospheric turbulence.<sup>10–14</sup> The isoplanatic, incoherent imaging systems are usually modeled as

\*Address all correspondence to Shiping Guo, E-mail: [sptguo@nwpu.edu.cn](mailto:sptguo@nwpu.edu.cn)

$$i(\mathbf{x}) = h(\mathbf{x}) \otimes o(\mathbf{x}) + n(\mathbf{x}), \quad (1)$$

where  $o(\mathbf{x})$  denotes the true target to be restored,  $i(\mathbf{x})$  is its observed data,  $n(\mathbf{x})$  denotes the additive photon noise,  $\otimes$  denotes the convolution, and  $h(\mathbf{x})$  predominantly denotes the atmospheric PSF.

Our goal is to estimate the true image of target  $o(\mathbf{x})$  based on the observation  $i(\mathbf{x})$ . In some applications, the PSF  $h(\mathbf{x})$  is usually unknown or partially unknown, causing the restoration to be an ill-posed problem. Over the past few decades, the vast majority of the research in blind restoration is concentrated in three different categories: (1) classical methods,<sup>4,5</sup> (2) statistical methods,<sup>6</sup> and (3) regularization methods.<sup>7,8</sup>

Classical methods primarily estimate image and PSF simultaneously in spatial and time domains, to achieve blind restoration through multiple iterations in constraint conditions. They mostly included Wiener filtering method, Richardson–Lucy (RL) method,<sup>3</sup> iterative blind deconvolution method (IBD),<sup>4</sup> and Richardson–Lucy iterative blind deconvolution (RLIBD) method. The RLIBD algorithm absorbs the advantages of simple calculation of the IBD method and takes into account the characteristics that the RL method maintains non-negative and energy conservation of the restored image. Although the RLIBD algorithm absorbs the advantages of the two methods, it fails to solve the PSF constraint problem and has a large number of iterations.

Statistical methods basically estimate the true image of a target by *priori* probability distribution of images and statistical model of noises. The *priori* probability models of images chiefly include generalized Gaussian model as well as Markov random field model. Statistical models of noises mainly include Poisson model and Gaussian model. The statistical methods mostly contain maximum-likelihood estimation, maximum *a posteriori* estimation (MAP), and expectation–maximization estimation.<sup>15–18</sup> The advantage of statistical methods is that they can easily add prior constraints and guarantee the existence and uniqueness of the solution. The disadvantage is that it is difficult to accurately find the prior probability model or the noise statistical model that accords with the actual situation. In addition, the algorithms have a large amount of computation as well as a slow convergence.

The basic ideas of regularization methods are to make use of the prior knowledge of the solution to construct constraints, so that the solution of the inverse problem can be determined. They mostly include total variational regularization and sparse regularization methods.<sup>7,19–21</sup> The regularization methods are mathematically equivalent to the statistical methods under the MAP framework in certain conditions. When solving the problem in an alternately iterative manner to a convergent solution, the regularization methods may employ the same or different optimization algorithms, but the final solution may not be global optimal solution.

Though various blind deconvolution algorithms have been proposed in past decades,<sup>22,23</sup> they face a variety of problems. The classical and regularization methods estimate PSF and true sharp images in an alternately iterative manner, leading to large computing time requirements due to slow convergence of the algorithm. The statistical methods are difficult to find image probability distribution and noise

statistical model accurately. In this paper, a neural network method based on cGAN is proposed for blind restoration of AO images. The cGAN method is an end-to-end blind restoration method without iterative computation and estimating PSF.

## 2.2 Generative Adversarial Network Method

GANs are a class of artificial intelligence algorithms used in unsupervised machine learning, implemented by a system of two neural networks, discriminator and generator, contesting with each other in a zero-sum game framework. They were introduced by Goodfellow et al.<sup>24</sup> This technique can generate images that look at least superficially authentic to human observers, having many realistic characteristics. The generator takes noise as an input and outputs a sample. The discriminator receives the sample image and a real image and tries to distinguish them. The goal of the generator is to fool the discriminator by generating perceptually convincing samples that cannot be distinguished from the real one. In the theoretical perspective, the game between the generator  $G$  and discriminator  $D$  is the minimax objective:

$$\min_G \max_D \mathbb{E}_{x \sim P_r} \{\log[D(x)]\} - \mathbb{E}_{\tilde{x} \sim P_g} \{\log[1 - D(\tilde{x})]\}, \quad (2)$$

where  $P_r$  is the distribution of original real data and  $P_g$  is the distribution of the generated samples, defined by  $\tilde{x} = G(z)$  and  $z \sim P(z)$ , the input  $\mathbf{z}$  is a random noise from the distribution  $P(z)$ . GAN was famous for its ability to generate samples of good perceptual quality.<sup>25</sup>

Recently, GANs have been applied to many different fields, such as cartoon image generation, face image generation, and music generation. But when dealing with image-to-image transformation problems, for example, image super-resolution, image style transfer, and image demosaics, GAN needs to be improved. Isola et al.<sup>9</sup> present cGAN architecture, which is also known as pix2pix. Unlike vanilla GAN, cGAN learns a mapping from observed image  $\mathbf{x}$  and random noise vector  $\mathbf{z}$  to  $\mathbf{y}$ , which can be expressed as  $G: \mathbf{x}, \mathbf{z} \rightarrow \mathbf{y}$ , where  $\mathbf{y}$  is the generated image. Thus, the generator's input is not just random noise, but the observation image  $\mathbf{x}$ . The discriminator supervises the training of the generator network by distinguishing the real target image and the generated image  $\mathbf{y}$ . Although Isola et al. demonstrated the perfect effect of cGAN for image-to-image transformation problems, no attempt has been made on the special problem of AO image blind restoration.

## 3 Method

Our purpose is to restore sharp images under the condition of known blurred observation and unknown PSF of atmosphere turbulence. Therefore, a generator network  $G_{\theta G}$  needs to be trained to estimate the sharp output image  $o(\mathbf{x})$  corresponding to per frame of blurred input  $i(\mathbf{x})$ . In addition, it also needs to introduce a discriminator network  $D_{\theta D}$  to train two networks in an adversarial manner to minimize the loss function and obtain the optimal network parameters.

### 3.1 Network Architecture

The generator network model used in this paper is shown in Fig. 1. The network is composed of an input convolution layer, two stride convolution layers with stride = 2, nine

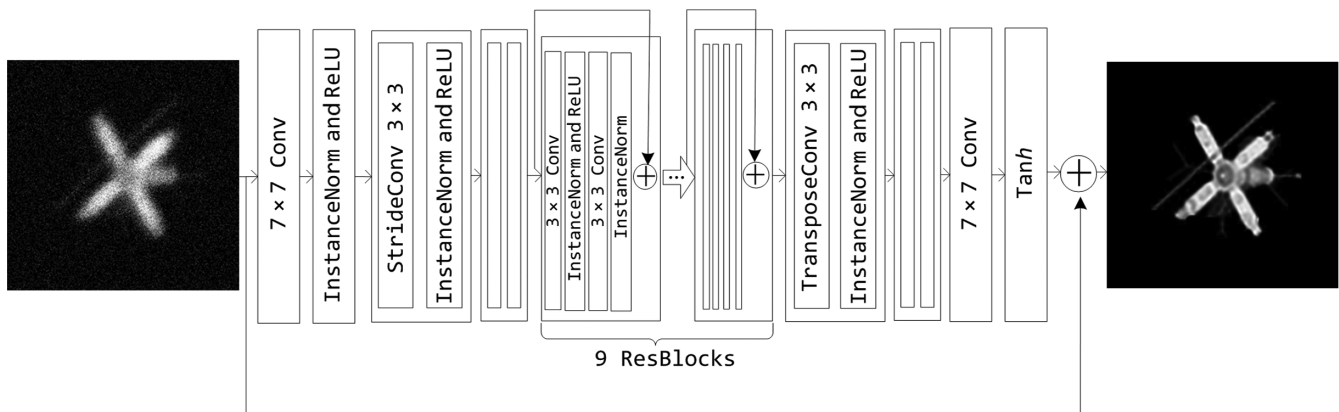


**Fig. 1** Generator network architecture. Constructing a CNN containing two stride convolution blocks with stride = 2, nine residual blocks, and two transposed convolution blocks. Each residual block consists of two convolution layers, two instance normalization layers, and an ReLU activation.

residual blocks, two transposed convolutional layers, and an output convolution layer. Each residual block is composed of two convolution layers, two instance normalization layers, and an ReLU activation layer. The ReLU activation function is defined as  $f(x) = \max(0, x)$ . Each convolution layer contains 256 filters and each filter contains 256 channels in residual block. That is, the residual block convolution layer is Conv2d [256, 256, kernel size = (3, 3), stride = (1, 1)]. In addition to the last output layer activation layer to select  $\tanh$  function, all other activation functions are ReLU function. The dropout regularization term with a probability of 0.5 was added after the first convolution layer in each residual block.<sup>9,26</sup> The number and size of convolution kernel in each convolution layer are also presented in Fig. 1.

In addition, a global skip connection was introduced in the generated network structure so that the residual

compensation image  $i(\mathbf{x})_R$ , corresponding to the blurred image by the generator network, can be directly added to the blurred image  $i(\mathbf{x})$ , that is

$$o(\mathbf{x}) = i(\mathbf{x}) + i(\mathbf{x})_R, \quad (3)$$

where  $o(\mathbf{x})$  is the final restored sharp image, which is ultimately generated by the generator network. It can be interpreted as that the residual network of the generator learned the compensation for atmospheric turbulence degradation. This design approach not only makes the training faster, but it also obtains better results.

In the training process, the Wasserstein distance with gradient penalty (WGAN-GP) was used to define the loss of the discriminator network  $D_{\theta D}$ . The  $D_{\theta D}$  network structure was similar to the PatchGAN<sup>9</sup> network structure, which contain

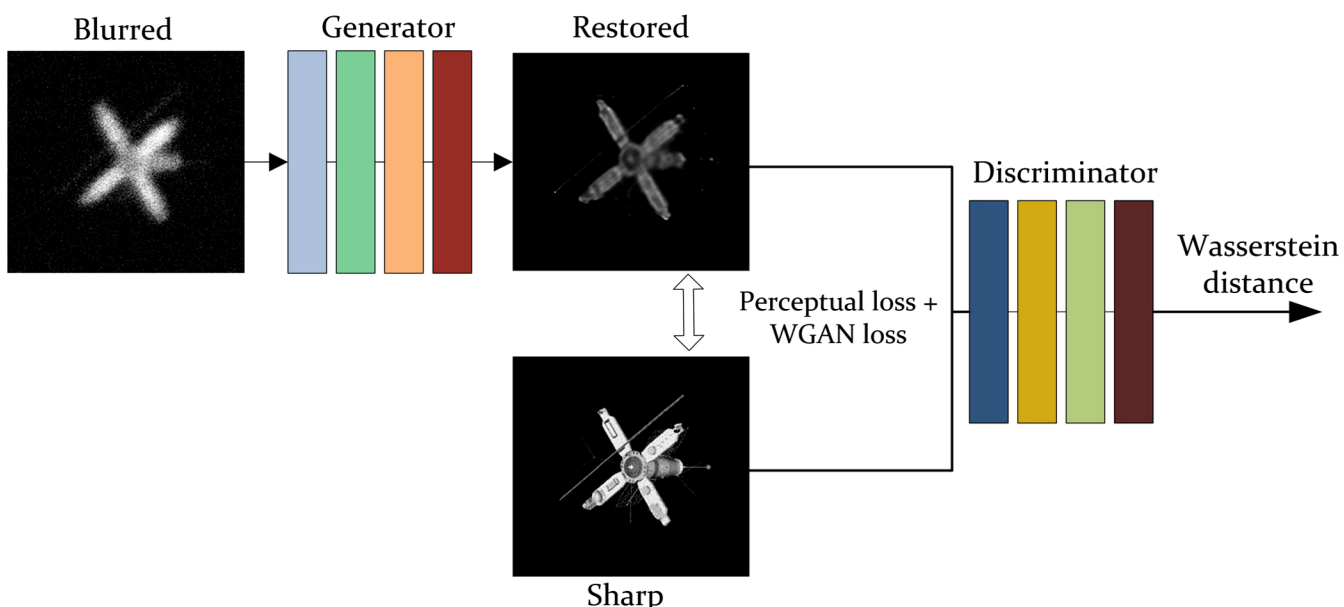


**Fig. 2** The flowchart of AO image restoration by cGAN. The generator network  $G_{\theta G}$  takes the degraded image as input and produces a corresponding sharp image. In the training process, the discriminator network  $D_{\theta D}$  takes the sharp image together with the original clear image as input to compute the distance between them. The total loss function contains the adversarial loss of discriminator and content loss of generator. When the training is over, only the generator network was used to restore the degraded image in the test.

$M$  convolutional layers and one fully connected layer. With the exception of the last convolutional layer, all convolutional layers are followed by an InstanceNorm layer and a Leaky-ReLU activation layer. The flowchart of AO image blind restoration by cGAN is displayed in Fig. 2.

### 3.2 Loss Function

The presented cGAN is an image-to-image system, which contains generator and discriminant networks. To ensure the convergence of the networks, we formulate the loss function as a combination of content loss  $L_X$  for generator network  $G_{\theta G}$  and adversarial loss  $L_{\text{GAN}}$  for discriminant network  $D_{\theta D}$

$$\mathcal{L} = \mathcal{L}_{\text{GAN}} + \lambda \cdot \mathcal{L}_X, \quad (4)$$

where  $\lambda$  indicates the weight coefficient, which is generally 100 in the experiment.

To make the reconstructed image and the sharp image consistent in both low-level pixel values and high-level visual perception, we proposed an improved content loss  $\mathcal{L}_X$  for generator network, which is composed of pixel loss and feature loss. The pixel loss is a simple L2-loss based on the difference of generated and target images. The feature loss is also L2-loss but is based on the difference of generated and target image convolutional neural network (CNN) feature maps. Therefore, content loss  $\mathcal{L}_X$  for generator network is defined as

$$\begin{aligned} \mathcal{L}_X &= \mathcal{L}_X^{\text{MSE}} + \mathcal{L}_X^{\text{VGG}_{i,j}} \\ &= \frac{1}{r_W r_H} \sum_{x=1}^{r_W} \sum_{y=1}^{r_H} \{o(\mathbf{x}) - G_{\theta G}[i(\mathbf{x})]\}^2 \\ &\quad + \frac{1}{W_{i,j} H_{i,j}} \sum_{x=1}^{W_{i,j}} \sum_{y=1}^{H_{i,j}} (\phi_{i,j}[o(\mathbf{x})] - \phi_{i,j}[G_{\theta G}[i(\mathbf{x})]])^2, \end{aligned} \quad (5)$$

where  $r_W$  and  $r_H$  represent the dimensions of the input image,  $\phi_{i,j}$  is the feature map obtained by the  $j$ 'th convolution before the  $i$ 'th max-pooling layer within VGG19 network, pretrained on ImageNet. Here,  $W_{i,j}$  and  $H_{i,j}$  denote the dimensions of the feature map.

The adversarial loss  $\mathcal{L}_{\text{GAN}}$  for discriminant network adopts the WGAN-GP proposed by Gulrajani et al.<sup>27</sup> This loss function not only solves the problem of training instability caused by gradient disappearance or gradient explosion but also provides a reliable indicator of the training process, and this indicator is highly correlated with the quality of the generated sample. Adversarial loss  $\mathcal{L}_{\text{GAN}}$  for discriminant network is defined as

$$\mathcal{L}_{\text{GAN}} = \sum_{n=1}^N -D_{\theta D}\{G_{\theta G}[i(\mathbf{x})]\}. \quad (6)$$

## 4 Dataset

To test our method for deblurring the space target images, we need large amounts of sharp-blur image pairs for training the cGAN. Literature research shows that there existed two public image restoration datasets for deep learning application, GoPro dataset<sup>28</sup> and Open Turbulent Image Set (OTIS).<sup>29</sup> GoPro dataset consists of 2103 pairs of blurred and sharp images, but it is a motion-blurred-type dataset, not suitable

for atmospheric turbulence degradation study. OTIS is a turbulence image dataset, but it is a horizontal path turbulence-degraded image set that still does not suit ground-based space target image restoration. In this section, we use two methods to simulate atmospheric degradation for constructing exclusive training dataset of space target images.

The atmospheric degradation wavefront under the condition of isoplanatic incoherent imaging is completely determined by the wavefront phase, which means that the simulation of PSF of the atmospheric degradation is equivalent to the numerical simulation for phase screen of atmospheric turbulence. The numerical simulation for phase screen mostly includes Zernike polynomial method and power spectrum inversion method.

### 4.1 Zernike Polynomial

This method expresses the atmospheric turbulence degradation wavefront as a linear combination of a series of orthogonal Zernike polynomials in circual domain.

$$\begin{cases} \phi(\vec{r}) = \sum_{k=1}^{\infty} a_k Z_k(\vec{r}) \\ a_k = \int W(\vec{r}) Z_k(\vec{r}) \phi(\vec{r}) d\vec{r}, \end{cases} \quad (7)$$

where  $W(\vec{r})$  equals  $1/\pi$  in the unit circle and equals 0 outside the circle;  $a_k$  is the coefficients of Zernike polynomial  $Z_k(\vec{r})$ , each  $Z_k(\vec{r})$  is called wavefront mode. Finally, the phase screen of atmospheric turbulence was calculated according to the above equation.

Figure 3 shows the phase screen of atmospheric turbulence and PSF by the Zernike polynomial method when the atmospheric turbulence strengths are 5, 10, and 15. We can find that with the turbulence intensity increasing, the distortion of the wavefront phase becomes more and more serious, and the PSF becomes more and more divergent.

### 4.2 Power Spectrum Inversion

The basic idea of power spectrum inversion method to generate random phase screen of atmospheric turbulence is as follows. First, a Gaussian random number matrix  $h(f_x, f_y)$  with zero mean and unit variance was generated in the frequency domain. Second, it is filtered by the power spectral density function  $\Phi_\varphi(f_x, f_y)$ , corresponding to the Kolmogorov spectrum of atmospheric turbulence. Finally, the Fourier transform was used to obtain the random phase screen of atmospheric turbulence  $\varphi(x, y)$ .

$$\begin{aligned} \varphi(\mathbf{x}, \mathbf{y}) &= \sum_{f_x} \sum_{f_y} h(f_x, f_y) \sqrt{\Phi_\varphi(f_x, f_y)} \exp[j(f_x \mathbf{x} \\ &\quad + f_y \mathbf{y})] \Delta f_x \Delta f_y, \end{aligned} \quad (8)$$

where  $\varphi(\mathbf{x}, \mathbf{y})$  and  $f_y$  are the space frequencies in the  $\mathbf{x}$  and  $\mathbf{y}$  directions, respectively. The power spectral density function  $\Phi_\varphi(f_x, f_y)$  is given as

$$\Phi_\varphi(f_x, f_y) = 0.023 r_0^{-5/3} f^{-11/3}, \quad (9)$$

where  $r_0$  is the atmospheric coherence length; it is a characteristic scale reflecting the intensity of the atmospheric turbulence.

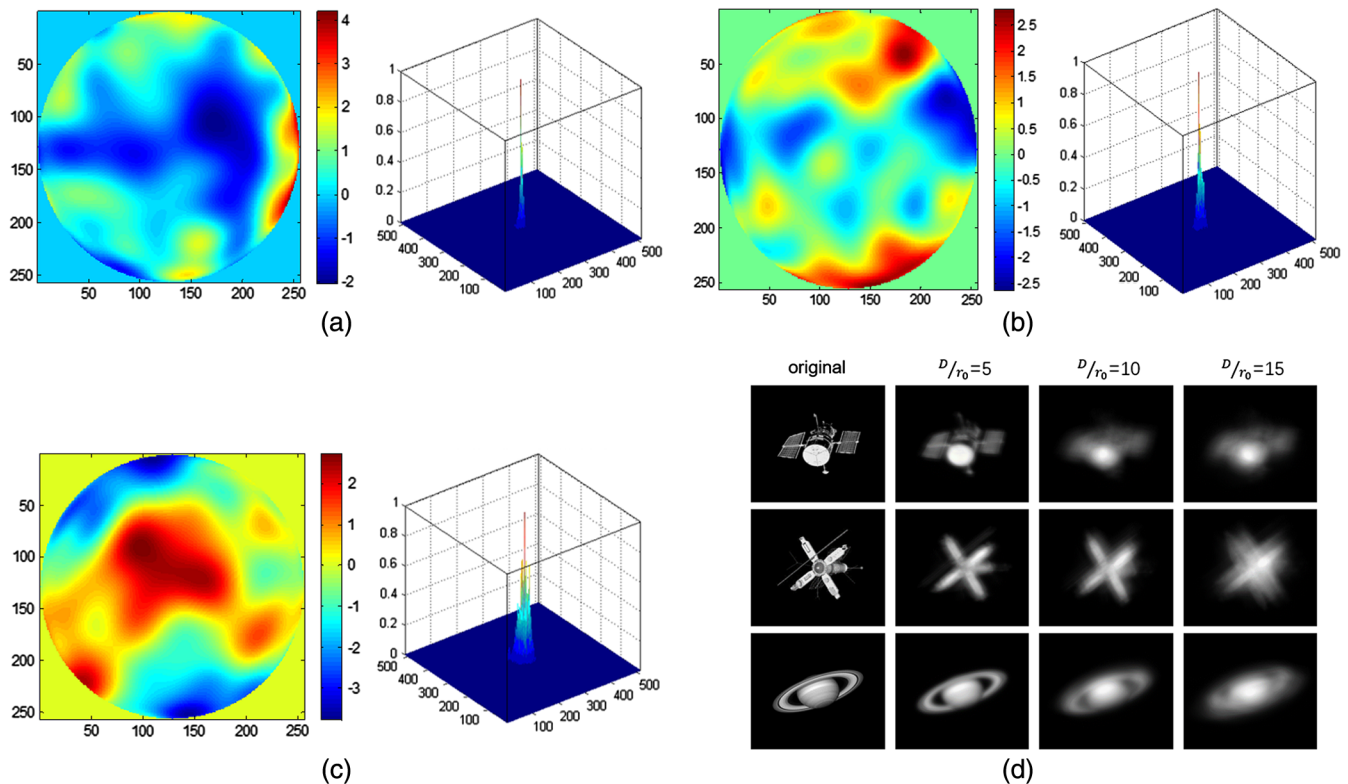


**Fig. 3** Zernike phase screen of atmospheric turbulence and PSF in different turbulence intensities. (a) The phase screen and PSF when  $D/r_0 = 5$ ; (b) the phase screen and PSF when  $D/r_0 = 10$ ; (c) the phase screen and PSF when  $D/r_0 = 15$ ; and (d) the simulation of degradation observation of different targets in different turbulence intensities.

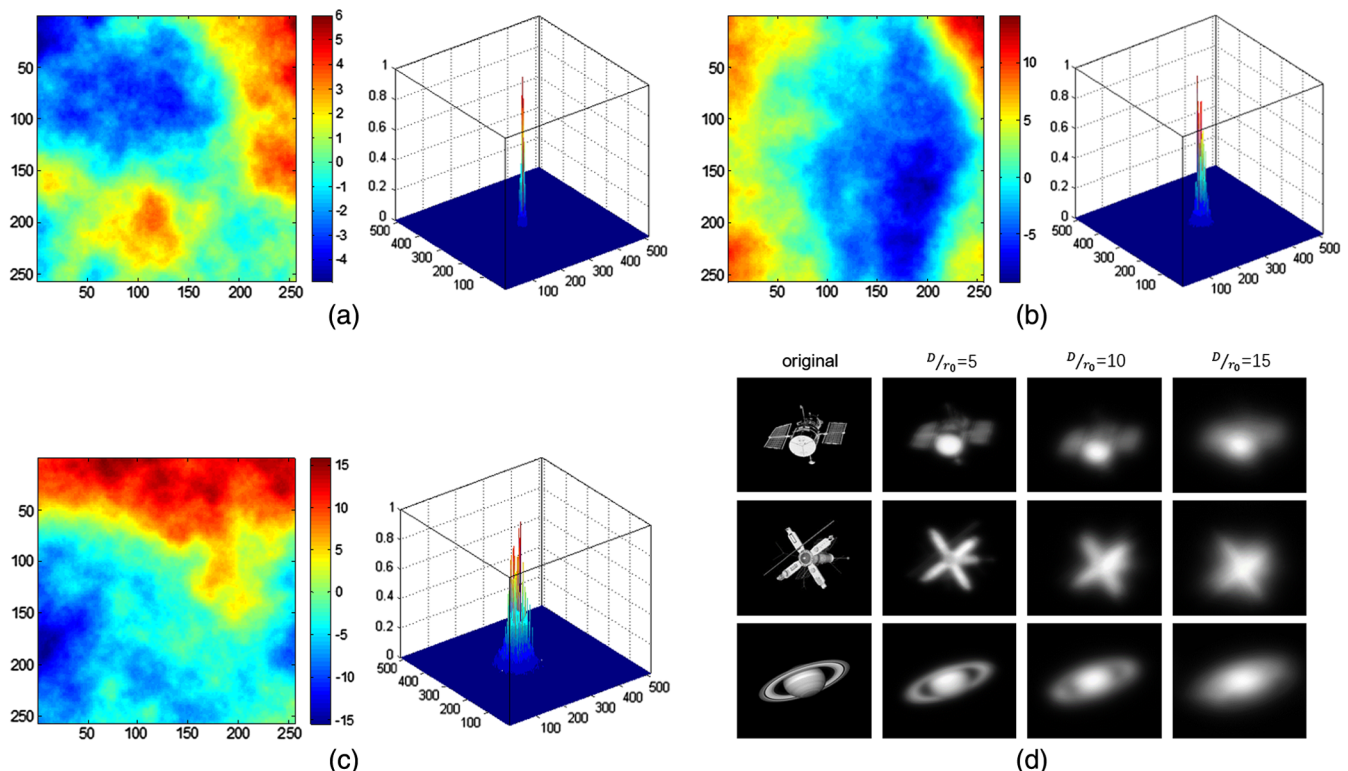


**Fig. 4** Power spectrum phase screen of atmospheric turbulence and PSF in different turbulence intensities. (a) The phase screen and PSF when  $D/r_0 = 5$ ; (b) the phase screen and PSF when  $D/r_0 = 10$ ; (c) the phase screen and PSF when  $D/r_0 = 15$ ; and (d) the simulation of degradation observation of different targets in different turbulence intensities.

Figure 4 shows the phase screen of atmospheric turbulence and PSF by power spectrum inversion method when the atmospheric turbulence strengths are 5, 10, and 15. The figure suggests that with the increase in turbulence intensity, the distortion of phase screen and the divergence of PSF become more and more serious.

Experimental results also indicated that the method of power spectrum inversion is better for simulating the degradation of high-frequency information, and the method of Zernike polynomial is better for simulating the degradation of low-frequency information. Therefore, the following section will use both of the methods simultaneously to construct our training dataset.

### 4.3 Constructing Dataset

The object of our study is AO images, which are two-dimensional images of space target and background information generated by AO CCD imaging system. In the imaging process, there are also noise effects in addition to

atmospheric turbulence. The noise mostly includes photon noise and electronic noise. When constructing the training dataset, we assume that the photon noise suits Poisson distribution and the electronic noise suits Gaussian distribution and add these noises to the simulated degraded images, respectively.

The procedure to construct the training dataset was as follows. (1) An original dataset containing 400 sharp images was constructed by rendering the existing three-dimensional (3-D) satellite models of 80 space targets with five different ground attitudes. (2) The original dataset was extended by applying data enhancement methods (mirroring and flipping), obtaining 1200 sharp images of space target. (3) Degradation simulations by Zernike polynomial method and power spectrum inversion method were conducted on the 1200 sharp images, respectively, under the atmospheric turbulence strengths of 5 and 10. As a result, we obtained 4800 blurred images of space targets. (4) Poisson and Gaussian white noises were added to the blurred images simultaneously. Finally, we got the training dataset containing 4800

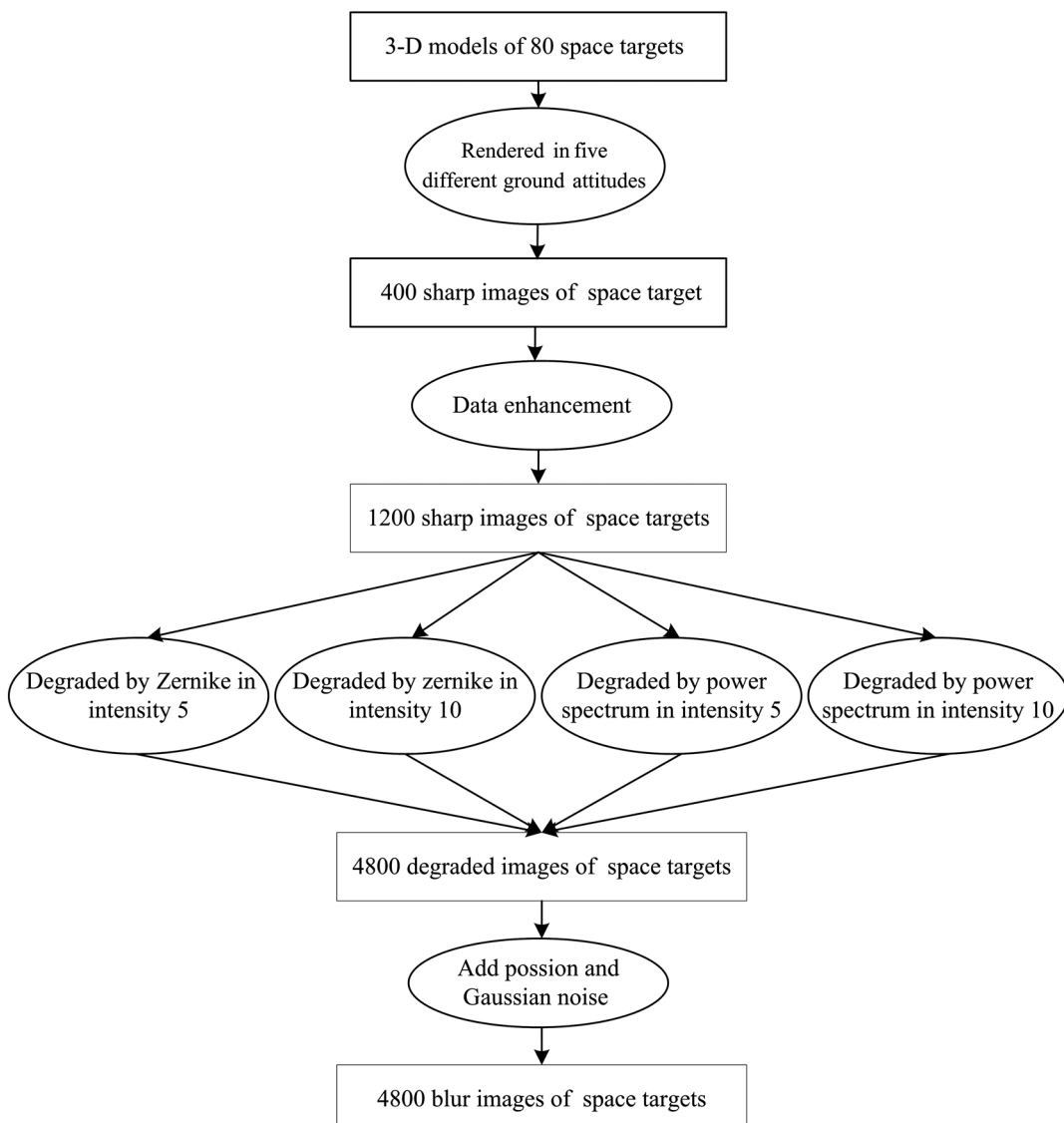


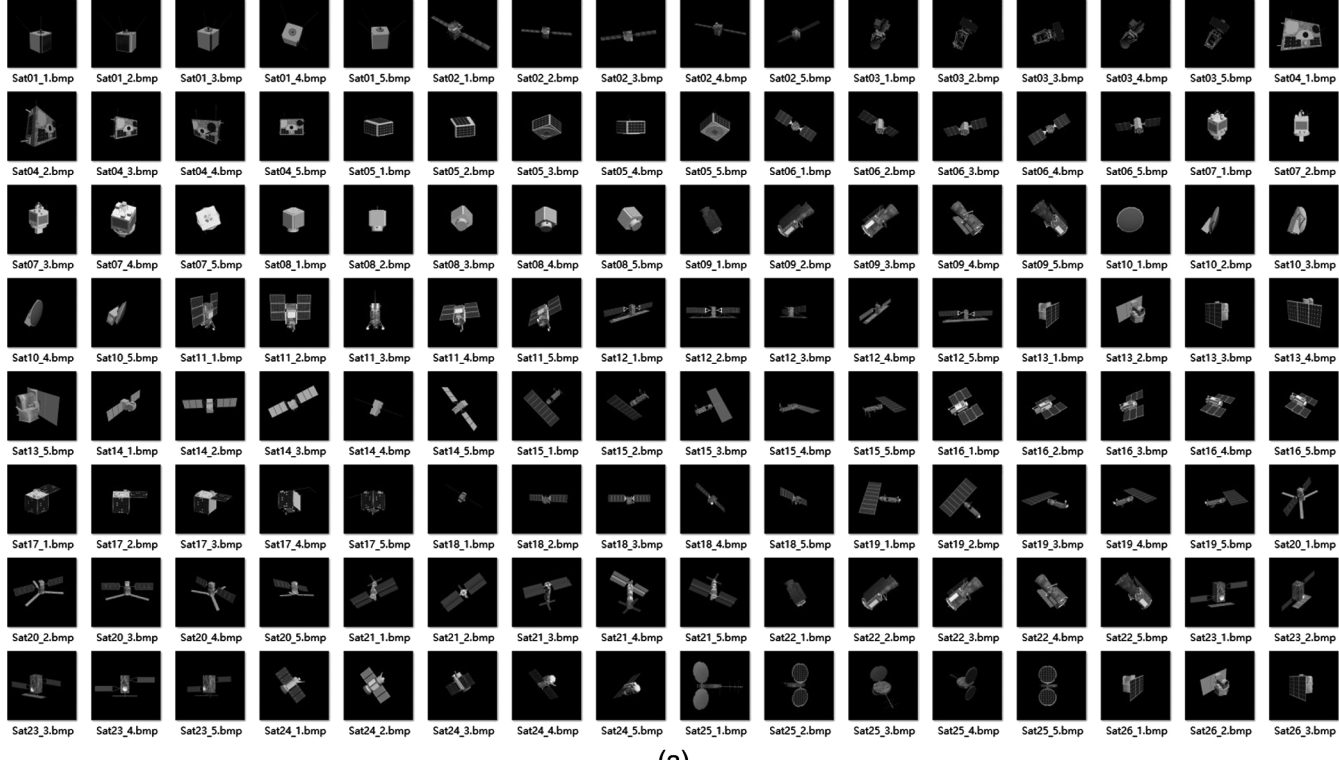
**Fig. 5** Flowchart of construction of the training dataset.

sharp-blur image pairs in  $512 \times 512$ . The flowchart of constructing the training dataset is shown in Fig. 5. Part of the training dataset is shown in Fig. 6. The test dataset is completely constructed from simulated images that are not included in the training dataset, as shown in Fig. 7.

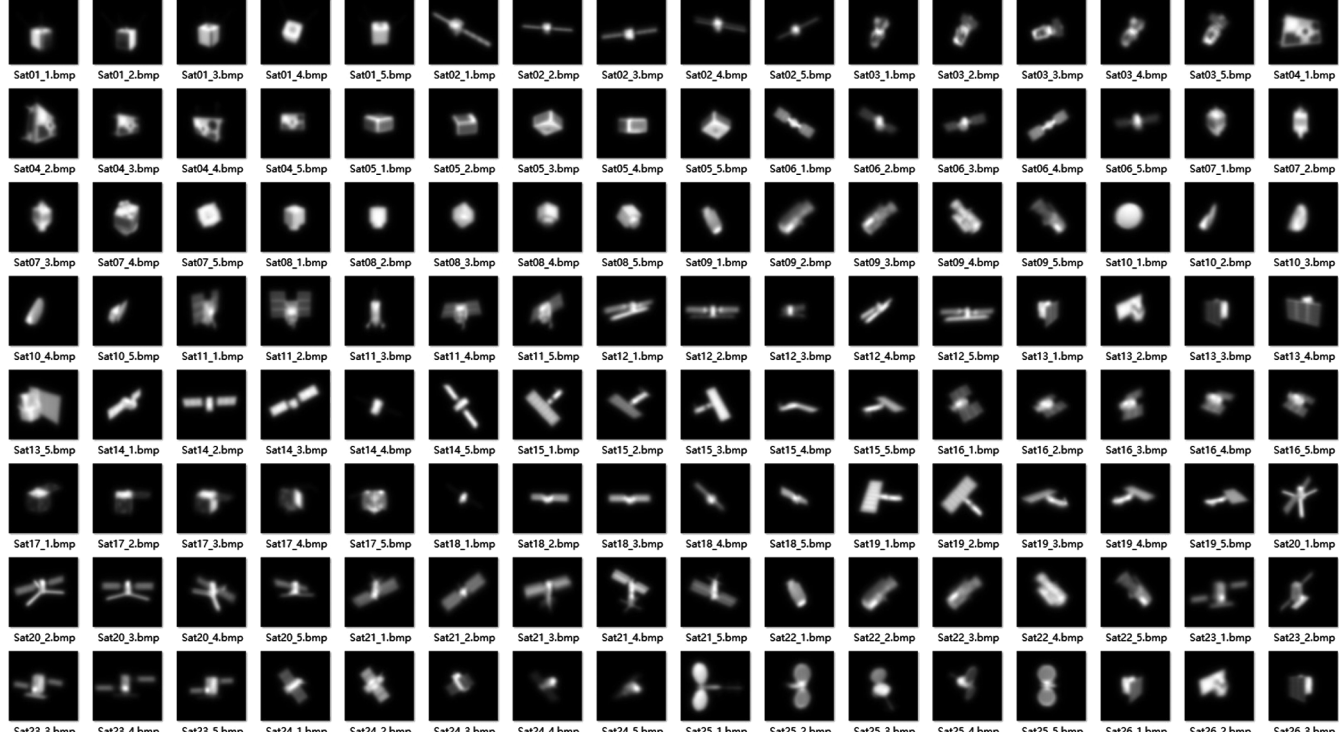
## 5 Experiments

### 5.1 Training

We implemented the algorithm proposed in this paper using PyTorch deep learning framework. The training platform



(a)



(b)

**Fig. 6** Part of the training dataset. (a) The sharp images and (b) the blurred images.

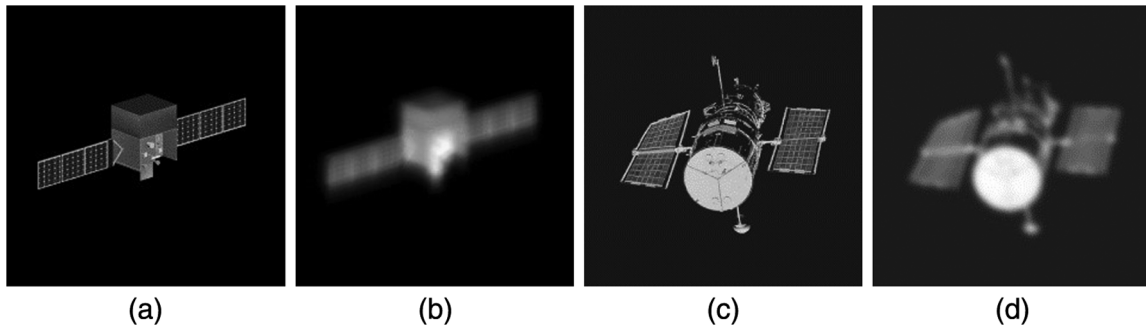


**Fig. 7** Part of the test dataset. (a) The sharp GLAST satellite image; (b) the corresponding blurred image by Zernike polynomial method in atmospheric turbulence strength  $D/r_0 = 10$ ; (c) the sharp Hubble satellite image; and (d) the corresponding blurred image by power spectrum inversion method in atmospheric turbulence strength  $D/r_0 = 10$ .

was on a single NVIDIA GTX 1080Ti GPU. The training dataset is the turbulent degradation blur–sharp image pairs of space target constructed in the previous section. The generator network input was a  $256 \times 256$ -image block. For optimization, we follow the approach of Ref. 27 and perform five gradient descent steps on  $D_{\theta D}$ , then one step on  $G_{\theta G}$ , using Adam as a solver. The initial learning rate of both networks was set to  $10^{-4}$ . After completing the training of the first 150 epochs, the learning rate was gradually reduced to 0 in the last 150 epochs. At test time, we follow the idea of Ref. 9 and apply both dropout and instance normalizations. All the models we trained with a batch size = 1 showed empirically better results on validation. The training phase took 7 days for training one cGAN network.

## 5.2 Evaluation Indicator

Before the experiments, we define two performance evaluation indicators: peak signal-to-noise ratio (PSNR) and structural similarity (SSIM).

PSNR is an objective measure of image quality, which represents the ratio of the maximum power of a signal-to-noise power that may affect its representation accuracy, that is, the ratio of the maximum signal-to-noise power, typically expressed in decibels (dB). The specific equation is as follows:

$$\text{PSNR} = 10 \cdot \log_{10} \left( \frac{\text{MAX}_I^2}{\text{MSE}} \right) = 20 \cdot \log_{10} \left( \frac{\text{MAX}_I}{\sqrt{\text{MSE}}} \right), \quad (10)$$

where

$$\text{MSE} = \frac{1}{mn} \sum_{i=0}^{m-1} \sum_{j=0}^{n-1} [I(i, j) - K(i, j)]^2, \quad (11)$$

where MSE represents the mean square error between two images,  $I(i, j)$  denotes a reference image, and  $K(i, j)$  denotes a noisy image that affects it. The larger the PSNR, the better the image quality.

SSIM is another measure of the similarity of two images, which defines image SSIM as a combination of three different factors: brightness, contrast, and structure. The mean is used as the estimate of the brightness, the standard deviation is used as the estimate of the contrast, and the covariance is used as a measure of the degree of SSIM. The specific equation is as follows:

$$\text{SSIM} = L(\mathbf{x}, \mathbf{y}) \times C(\mathbf{x}, \mathbf{y}) \times S(\mathbf{x}, \mathbf{y}), \quad (12)$$

$$L(\mathbf{x}, \mathbf{y}) = \frac{2\mu_x\mu_y + c_1}{\mu_x^2 + \mu_y^2 + c_1}, \quad (13)$$

$$C(\mathbf{x}, \mathbf{y}) = \frac{2\sigma_x\sigma_y + c_2}{\sigma_x^2 + \sigma_y^2 + c_2}, \quad (14)$$

$$S(\mathbf{x}, \mathbf{y}) = \frac{\sigma_{xy} + c_3}{\sigma_x\sigma_y + c_3}, \quad (15)$$

where  $\mathbf{x}$  and  $\mathbf{y}$  denote the two images,  $L(\mathbf{x}, \mathbf{y})$  denotes the brightness factor,  $C(\mathbf{x}, \mathbf{y})$  denotes the contrast factor, and  $S(\mathbf{x}, \mathbf{y})$  denotes the structural factor. Here,  $\mu_x$  is the mean of  $\mathbf{x}$ ;  $\mu_y$  is the mean of  $\mathbf{y}$ ;  $\sigma_x^2$  is the variance of  $\mathbf{x}$ ;  $\sigma_y^2$  is the variance of  $\mathbf{y}$ ;  $\sigma_{xy}$  is the covariance of  $\mathbf{x}$ ; and  $\mathbf{y}$ ,  $c_1$ ,  $c_2$ , and  $c_3$  are the constants used to maintain stability. When  $c_3 = c_2/2$ , then

$$\text{SSIM} = \frac{(2\mu_x\mu_y + c_1)(2\sigma_x\sigma_y + c_2)}{(\mu_x^2 + \mu_y^2 + c_1)(\sigma_x^2 + \sigma_y^2 + c_2)}. \quad (16)$$

The larger the SSIM, the higher the similarity between the two images. In extreme cases, when the two images are identical, the value is equal to 1.

## 5.3 Test and Analysis

In this section, the performance of cGAN was tested on the test dataset in Fig. 7. The blurred GLAST image was degraded by Zernike polynomial method in turbulence intensity  $D/r_0 = 10$  and the blurred Hubble image was degraded by power spectrum inversion method in the same turbulence intensity. Then, Poisson noise and Gaussian noise with a variance of  $\sigma^2 = 0.01$  were added to the degraded images to simulate the photon noise and the electronic noise, respectively.

To compare with the proposed algorithm, we choose the algorithm of better performance in the project application. They are last nonlinear Wiener filter (last-NLW),<sup>30</sup> RLBD, and expectation–maximization iteration blind deconvolution algorithm (EMIBD).

Figure 8 shows the result of blind restoration for GLAST image by four different algorithms. The sharpness of the restored images was higher than the degraded ones, and some important high-frequency information of the original

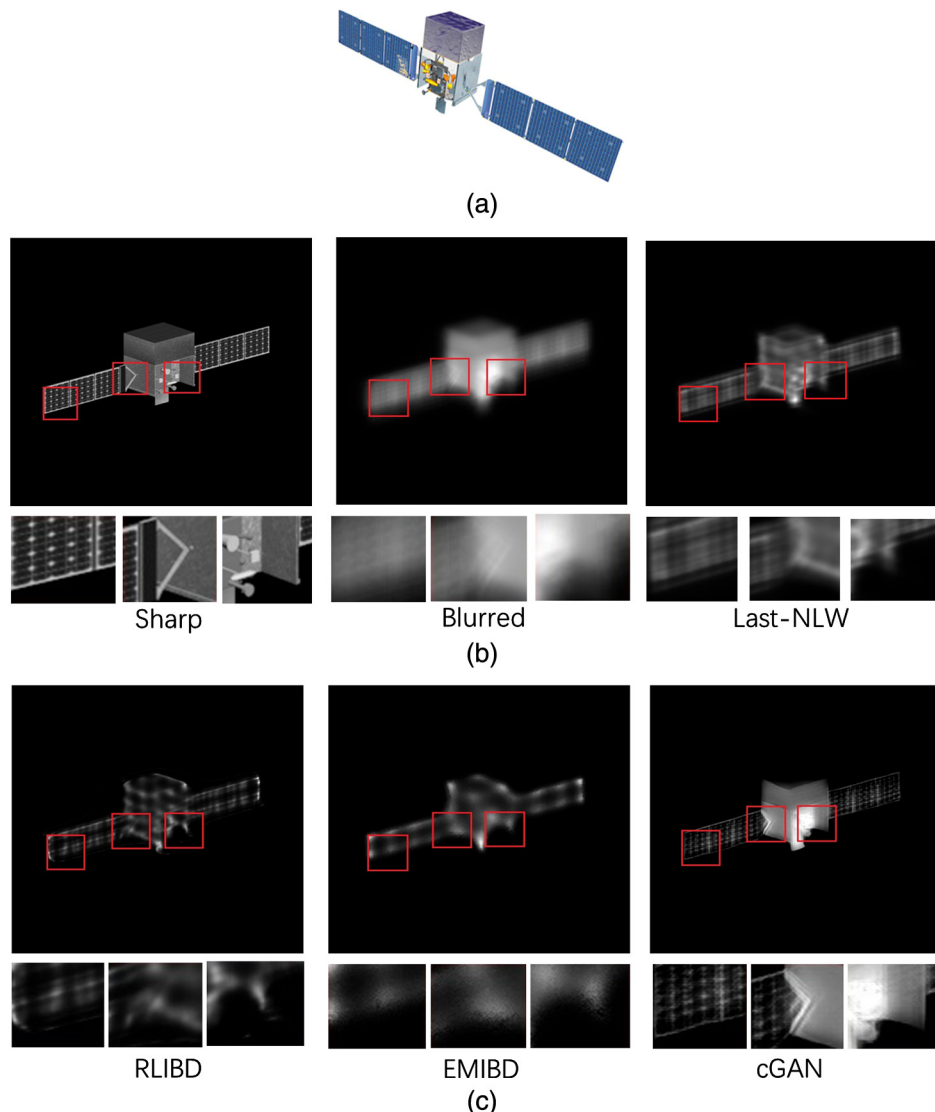


**Fig. 8** The results of blind restoration for GLAST by four different restoration methods. (a) The model of GLAST; (b) the sharp image, the blurred image by Zernike polynomial method in atmospheric turbulence strength  $D/r_0 = 10$  and the result of restoration by last-NLW; (c) the results of restoration by RLBD, EMIBD, and cGAN, respectively.

image could be restored in a sense. When the four methods were compared with each other, we could find that the cGAN had better performance on geometric contours and edge structures by the detail enlargement in Fig. 8, such as solar panels and connection parts. Therefore, the cGAN is better for AO images than that of last-NLW, RLBD, and EMIBD. The indicator evaluation of the four methods given in Table 1 also verified the subjective visual evaluation again. It could be seen that cGAN was superior to last-NLW, RLBD, and EMIBD in PSNR and SSIM. It may be due to the fact that the generator had learned the turbulent degradation process and compensated the AO imaging losses by supervised training. It was important to point out that as last-NLW, RLBD, and EMIBD all used alternatively iterations to estimate the sharp image and PSF, they cost more time to restore single-frame image. Though the cGAN took a long time to train the neural network parameters, the efficiency of restoring single-frame image was acceptable in testing. The time consumption of four methods for restoring a single frame of a GLAST image

**Table 1** Mean of PSNR and SSIM on four different methods and computation cost on single-frame GLAST image.

GLAST	PSNR	SSIM	Time
RLBD	48.3	0.8820	3 min 22 s
EMIBD	47.1	0.88	5 min 6 s
Last-NLW	48.4	0.8913	2 min 28 s
cGAN	<b>48.5</b>	<b>0.8922</b>	<b>3.9 s</b>

Note: The bold values represent the best values.

was given in the right-most column of Table 1. (The best iterations number of RLBD is 524.) It could be seen that cGAN had a better restoration accuracy; apart from this, it had an order of magnitude improvement in efficiency, and computation cost reduced from minute to second.

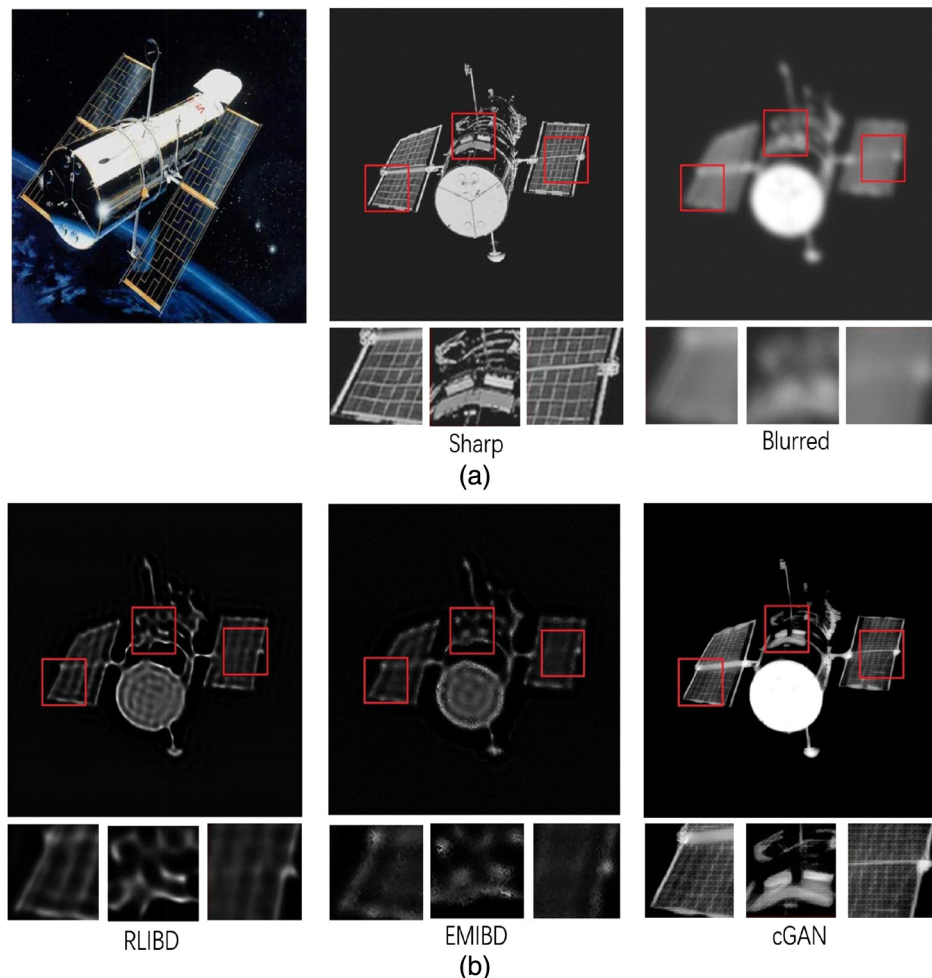


**Fig. 9** The results of blind restoration for Hubble by three different restoration methods. (a) The model, the sharp image, and the blurred image by power spectrum inversion method in atmospheric turbulence strength  $D/r_0 = 10$ ; (b) the results of restoration by RLBD, EMIBD, and cGAN, respectively.

Figure 9 displays the result of blind restoration for Hubble image by three different methods. It could be seen that the quality of the restored images were improved in a way that the three methods as well as the performance of cGAN was most obvious. It not only accurately recovered the geometric contour of the image but also had remarkably improved some high-frequency details. This may be because the cGAN network had mastered the distribution of satellite images by learning 4800 pairs of training datasets. Table 2 gives the quantitative performance evaluation. (The best iterations number of RLBD is 132.) It could be seen that the cGAN method had the largest values in the indicator of SSIM and

PSNR. The subjective visual evaluation by Fig. 9 verified this result. At the same time, the computation time for restoring a single-frame image is given in the right column of Table 2. The method of cGAN costs the shortest time because of its output was only the restored sharp image without estimating PSF. The RLBD and EMIBD both needed to estimate the sharp image and PSF in an alternately iterative manner under the constraint conditions, taking a long time.

To verify the robustness of cGAN method, the degraded GLAST images by Zernike polynomial method in different turbulence intensities were used to test the proposed method. Figure 10 shows the PSNR curves of the blurred image and restored images by cGAN and RLBD, respectively, in different atmospheric turbulence strengths. The figure suggested the following four solutions. First, with the increase of atmospheric turbulence strength, image blur was aggravated. Second, the improvement of image quality by cGAN was obvious in PSNR indicator. Third, the accuracy of restoration by cGAN is better than that of RLBD in different turbulence intensity. Finally, the cGAN method proposed in this paper was satisfactory for restoration of degraded images in medium and weak turbulent intensities. With the increase of turbulence intensity, the improvement of image quality was limited.

**Table 2** Mean PSNR and SSIM on three different methods and the computation cost on single-frame Hubble image.

Hubble	PSNR	SSIM	Time
RLBD	35.3	0.3742	7 min 18 s
EMIBD	31.2	0.1867	21 min 54 s
cGAN	<b>37.2</b>	<b>0.6480</b>	<b>3.7 s</b>

Note: The bold values represent the best values.

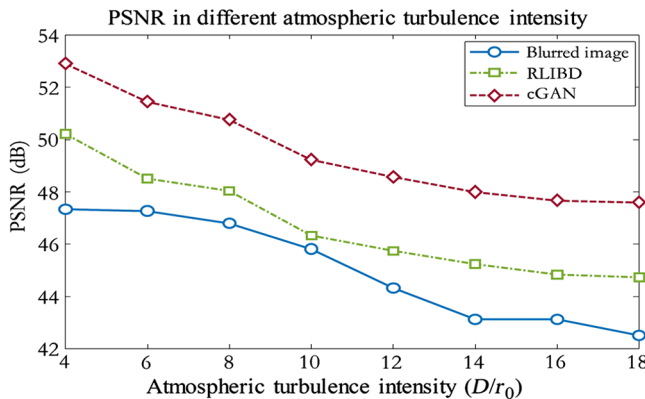


**Fig. 10** The mean PSNR of restored GLAST image by RLIBD and cGAN in different atmospheric turbulence strengths.

To demonstrate the robustness of the cGAN method more intuitively, Fig. 11 shows the restored GLAST images by RLIBD and cGAN in different atmospheric turbulence strengths. It could be seen clearly that, with the increase of turbulence intensity, the cGAN method was still effective as well as had better restoration accuracy than RLIBD.

Accordingly, we concluded that cGAN was robust in medium and weak turbulent intensities.

## 6 Conclusion

In this paper, we presented a blind restoration method for AO images based on cGAN, which is a supervised neural network including a generator and a discriminator. The cGAN was used to learn the process of turbulent degradation and compensate the losses of AO imaging. In addition, we implemented two simulation methods of atmospheric turbulence for constructing a ground-based space target image dataset. The dataset used to train neural network is composed of 4800 blur-sharp image pairs by rendering the existing 3-D satellite models of 80 space targets. We introduced an improved loss function that combined the pixel loss and feature loss for optimizing the network parameters quickly and steadily.

The comprehensive experimental analysis suggested that the cGAN method proposed in this paper is satisfactory for medium and weak turbulent intensities. Subjective visual evaluation showed that the geometric contour of space targets and even the fine structures on edge had been recovered accurately. Objective index evaluation further verified the

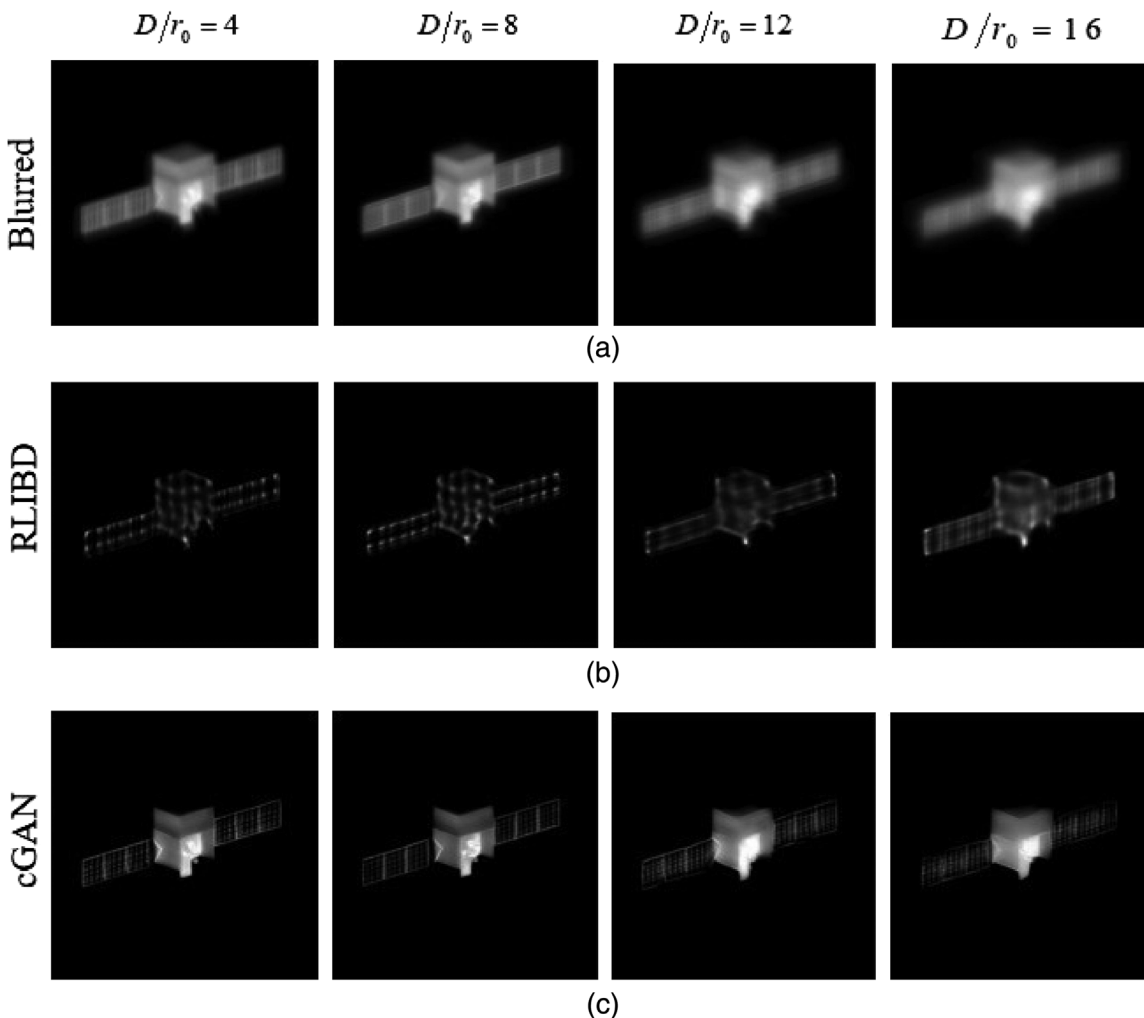


**Fig. 11** Results of the restored GLAST images by RLIBD and cGAN in different atmospheric turbulence strengths. (a) The blurred images, (b) the restored images by RLIBD, and (c) the restored images by cGAN.

performance improvements. From the Hubble satellite restoration result, we saw that the PSNR had improved nearly 15%, the SSIM had increased  $\sim 2$  to 3 times, and what is more, the computation cost had an order of magnitude improvement from dozens of minutes decreased to several seconds. When atmospheric turbulence strength is stronger, the restoration accuracy of cGAN algorithm can be still better than that of the comparison ones. In future work, designing more specialized network architecture for atmospheric turbulence degradation is worthy of further study.

### Acknowledgments

This work was supported by the National Natural Science Foundation of China (No. 61179010), the Fundamental Research Funds for the Central Universities (No. G2017KY0310), and the National Key Research and Development Program of China (No. 2016YFB0501301). The authors declare that there are no conflicts of interest related to this article.

### References

1. P. Campisi and K. Egiazarian (Eds.), *Blind Image Deconvolution: Theory and Applications*, CRC Press, Taylor & Francis Group, Boca Raton, London, New York (2016).
2. D. Kundur and H. Dimitrios, "Blind image deconvolution revisited," *IEEE Signal Process. Mag.* **13**(6), 61–63 (1996).
3. W. H. Richardson, "Bayesian-based iterative method of image restoration," *J. Opt. Soc. Am. A* **62**(1), 55–59 (1972).
4. G. R. Ayers and J. C. Dainty, "Iterative blind deconvolution method and its applications," *Opt. Lett.* **13**(7), 547 (1988).
5. M. Prato, A. L. Camera, and S. Bonettini, "A convergent blind deconvolution method for post-adaptive-optics astronomical imaging," *Inverse Prob.* **29**(6), 065017 (2013).
6. A. K. Atsaggelos and K. T. Lay, "Maximum likelihood blur identification and image restoration using the EM algorithm," *IEEE Trans. Signal Process.* **39**(3), 729–733 (1991).
7. S. Guo et al., "Multichannel parallel deblurring and collaborative registration using Gaussian total variation regularization for image fusion," *Math. Prob. Eng.* **2016**, 1–10 (2016).
8. L. Yan, H. Fang, and S. Zhong, "Blind image deconvolution with spatially adaptive total variation regularization," *Opt. Lett.* **37**(14), 2778–2780 (2012).
9. P. Isola et al., "Image-to-image translation with conditional adversarial networks," in *IEEE Conf. Comput. Vision and Pattern Recognit.*, pp. 5967–5976 (2017).
10. M. H. Furhad, M. Tahtali, and A. Lambert, "Restoring atmospheric-turbulence-degraded images," *Appl. Opt.* **55**(19), 5082–5090 (2016).
11. D. Shi et al., "Reconstruction of spatially misaligned and turbulence degraded images," *Opt. Lasers Eng.* **50**(5), 703–709 (2012).
12. X. Fei et al., "Deblurring adaptive optics retinal images using deep convolutional neural networks," *Biomed. Opt. Express* **8**(12), 5675–5687 (2017).
13. A. S. Carasso et al., "APEX blind deconvolution of color Hubble Space Telescope imagery and other astronomical data," *Opt. Eng.* **45**(10), 107004 (2006).
14. H. Gong et al., "Holographic imaging with a Shack–Hartmann wave-front sensor," *Opt. Express* **24**(13), 13729–13737 (2016).
15. C. L. Matson et al., "Fast and optimal multiframe blind deconvolution algorithm for high-resolution ground-based imaging of space objects," *Appl. Opt.* **48**(1), A75–A92 (2009).
16. L. Li et al., "Learning a discriminative prior for blind image deblurring," in *Proc. IEEE Conf. Comput. Vision and Pattern Recognit.*, pp. 6616–6625 (2018).
17. R. B. Gallé et al., "Blind deconvolution of turbulence-degraded images using natural PSF priors," in *Imaging and Appl. Opt.* (2014).
18. J. G. Nagy et al., "Space-varying restoration of optical images," *J. Opt. Soc. Am. A* **14**(12), 3162–3174 (1997).
19. Y. V. Zhu, "Multiframe blind deconvolution of heavily blurred astronomical images," *Appl. Opt.* **45**(28), 7342–7352 (2006).
20. Q. Yin et al., "Blind deconvolution for astronomical spectrum extraction from two-dimensional multifiber spectrum images," *Opt. Express* **25**(5), 5133–5145 (2017).
21. D. Li, R. M. Mersereau, and S. Simske, "Atmospheric turbulence-degraded image restoration using principal components analysis," *IEEE Geosci. Remote Sens. Lett.* **4**(3), 340–344 (2007).
22. J. Lucas, B. Calef, and T. Kyono, "Recovering astronomical images with deep neural network supported bispectrum processing" in *Adv. Maui Opt. and Space Survill. Technol. Conf.* (2018).
23. Z. Gao, C. Shen, and C. Xie, "Stacked convolutional auto-encoders for single space target image blind deconvolution," *Neurocomputing* **313**, 295–305 (2018).
24. I. Goodfellow et al., "Generative adversarial nets," in *Adv. Neural Inf. Process. Syst.*, pp. 2672–2680 (2014).
25. C. Schuler et al., "Learning to deblur," *IEEE Trans. Pattern Anal. Mach. Intell.* **38**(7), 1439–1451 (2016).
26. T. Salimans et al., "Improved techniques for training GANs," in *Adv. Neural Inf. Process. Syst.*, pp. 2234–2242 (2016).
27. I. Gulrajani et al., "Improved training of Wasserstein GANs," in *Adv. Neural Inf. Process. Syst.*, pp. 5767–5777 (2017).
28. S. Nah, T. Kim, and K. Lee, "Deep multi-scale convolutional neural network for dynamic scene deblurring," in *IEEE Conf. Comput. Vision Pattern Recognit.* Vol. 1, No. 2, p. 3 (2017).
29. J. Gilles and N. Ferrante, "Open turbulent image set (OTIS)," *Pattern Recognit. Lett.* **86**, 38–41 (2017).
30. D. Gerwe et al., "Regularization for nonlinear image restoration using a prior on the object power spectrum," *Proc. SPIE* **5896**, 589604 (2005).

**Jianglin Shi** is a PhD candidate at Xi'an Jiaotong University, Xi'an, China. He received his MS degree in control science and engineering from Xi'an Jiaotong University in 2016. His current research interests include adaptive optics (AO) image restoration and space target detection and identification.

**Rongzhi Zhang** received his PhD from Northwestern Polytechnical University, Xi'an, China, in 1999. Currently, he is a senior engineer and research fellow at Xi'an Satellite Control Center, Xi'an, China. His main research areas include orbital dynamics and space target detection and recognition.

**Shiping Guo** received his PhD from Xi'an Jiaotong University, Xi'an, China, in 2017. Currently, he is an assistant professor at Northwestern Polytechnical University, Xi'an, China. His main research areas include AO image restoration and space target detection and identification.

**Yikang Yang** received his PhD in control science and engineering from Xi'an Jiaotong University in 2003. Currently, he is a professor at the Systems Engineering Institute, Xi'an Jiaotong University, Xi'an, China. His research interests are in space communication, intrasatellite networks, and Global Navigation Satellite System signal processing.

**Rong Xu** received her master's degree from Nanjing University of Science and Technology, Nanjing, China, in 1998. Currently, she is a senior engineer at Xi'an Satellite Control Center, Xi'an, China. Her main research interests include photoelectric measurement and AO.

**Wei Niu** received his master's degree from the National University of Defense Technology, Changsha, China, in 2005. Currently, he is a senior engineer and a PhD candidate at Xi'an Jiaotong University, Xi'an, China. His main research interests include space target detection and identification.

**Jisheng Li** received his BEng degree in celestial mechanics from Nanjing University, Nanjing, China, in 1966. Currently, he is a professor at the Systems Engineering Institute, Xi'an Jiaotong University, Xi'an, China, and academician at the Chinese Academy of Sciences, Beijing, China. His main research areas include astrodynamics, geophysics, and aerology.